Histological and cytological imaging using Fourier ptychographic microscopy

Bendkowski, Christopher, Fu, Bin, Manescu, Petru, Claveau, Rémy, Fernandez-Reyes, Delmiro, et al.

Christopher Bendkowski, Bin Fu, Petru Manescu, Rémy Claveau, Delmiro Fernandez-Reyes, Michael Shaw, "Histological and cytological imaging using Fourier ptychographic microscopy," Proc. SPIE 11879, Frontiers in Biophotonics and Imaging, 1187902 (6 October 2021); doi: 10.1117/12.2604455

SPIE.

Event: SPIE Photonex, 2021, Glasgow, Scotland, United Kingdom

Histological and Cytological Imaging using Fourier Ptychographic Microscopy

Christopher Bendkowski[a], Bin Fu[b], Petru Manescu[a], Rémy Claveau[c], Delmiro Fernandez-Reyes[a], Michael Shaw*[a,d]

[a]Department of Computer Science, Faculty of Engineering Sciences, University College London, 66–72 Gower Street, London, WC1E 6EA, UK; [b]Department of Chemistry, University of Cambridge, Lensfield Road, Cambridge, CB2 1EW, UK; [c]ICube laboratory, Université de Strasbourg (CNRS), UMR 7357, 300 Boulevard Sébastien Brant, 67460 Illkirch Graffenstaden, France; [d]Department of Chemical and Biological Sciences, National Physical Laboratory, Teddington, Middlesex, TW11 0LW, UK

ABSTRACT

Structural imaging using light microscopy is a cornerstone of histology and cytology. However, the utility of the optical microscope for diagnostic imaging is limited by the fundamental tradeoff between the field of view and spatial resolution and a reliance on exogenous dyes to generate sufficient image contrast. Fourier Ptychographic Microscopy (FPM) is a complex imaging modality with the potential to overcome these limitations by recovering high-resolution images of sample amplitude and phase from a set of low-resolution raw images captured under inclined illumination. In this article we explore the application of FPM to clinical imaging using a simple, low-cost FPM system and simulated and experimental data to explore the influence of both image acquisition parameters and hardware configuration on image quality and imaging throughput. The practical performance of the method is investigated by imaging peripheral blood films and histological tissue sections. We find that, at the cost of increased computational complexity, FPM increases the information capture capacity of the optical microscope significantly, allowing label-free examination and quantification of features such as tissue and cell morphology over large sample areas.

Keywords: optical microscopy, Fourier ptychographic microscopy, biomedical imaging, computational imaging, quantitative phase imaging, digital pathology

1. INTRODUCTION

The capacity of light microscopy for minimally invasive high-resolution imaging has been fundamental in the development of our understanding of biological systems and processes. In clinical pathology, analysis of images from brightfield optical microscopes remains the gold standard for the diagnosis of diseases from cancers to blood borne infections. However, the ability of an optical microscope to capture diagnostically relevant structural information from biomedical samples is limited by a number of fundamental physical and practical engineering constraints. Firstly, limits to the size of most microscope objectives results in a trade-off between the numerical aperture (NA) and the microscope's magnification. This means the microscopist must make a compromise between spatial resolution and the volume of a sample which can be visualized in a single image field. Secondly, although there are range of label free optical imaging modalities, from phase imaging[1] to label free chemical imaging techniques[2], most clinical microscopes in use today are simple brightfield systems which rely on the addition of exogenous chromophores, such as haemotoxylin and Eosin (H&E), to differentially stain sample features and provide image contrast. Whilst offering advantages in terms of specificity, staining procedures add time and complexity to the

*mike.shaw@ucl.ac.uk

Frontiers in Biophotonics and Imaging, edited by Sumeet Mahajan, Stefanie Reichelt, Proc. of SPIE Vol. 11879, 1187902 · © 2021 SPIE · CCC code: 0277-786X/21/$21 · doi: 10.1117/12.2604455

clinical workflow, can introduce unwanted artefacts and typically render the sample unsuitable for further downstream biochemical analysis.

Fourier Ptychographic Microscopy[3] is a computational optical imaging technique with the potential to overcome some of these limitations by allowing the recovery of a high resolution, complex image using a low magnification, low NA objective lens. FPM relies on inclined illumination to shift the region of the sample spectrum captured by the microscope. Typically, a series of images is recorded as the sample is illuminated at different angles using individually addressable LEDs in a 2D matrix. This image series is then combined using iterative phase retrieval[4] to recover a high-resolution estimate of the sample phase (optical path length) and amplitude. In this article we investigate the application of FPM to cytological and histological imaging using a simple, low-cost FPM system to image Giemsa-stained peripheral blood films and stained and unstained histological tissue sections. Using a combination of simulated and experimental image data we explore the effects of hardware configuration and image reconstruction parameters on the quality of reconstructed images and imaging throughput. Based on our results we discuss the potential for broader clinical application of FPM.

2. FOURIER PTYCHROGRAPHIC MICROSCOPE SYSTEM

2.1 FPM theory

When a thin object with complex transmittance $t(x,y)$ is illuminated by a monochromatic plane wave $e_i(x,y) = e^{i(k_0(\alpha_i x+\beta_i y))}$, the wave exiting the sample is given by $e_o(x,y) = t(x,y)e_i(x,y)$, where k_0, (x,y) and (α_i,β_i) are the wavenumber of the illumination, the coordinates in the sample plane and the illumination angle respectively. In an optical microscope the spectrum of this exit wave, $E\left(k_x,k_y\right)$, where $\left(k_x,k_y\right)$ are spatial frequencies, is multiplied by the pupil function of the objective lens $P\left(k_x,k_y\right)$ with the final (intensity) image at the camera given by

$$I_i = \left|\mathcal{F}^{-1}\left[P\left(k_x,k_y\right)E\left(k_x,k_y\right)\right]\right|^2, \tag{1}$$

where the $\mathcal{F}^{-1}$ is the inverse Fourier transform operator. For an ideal aberration-free coherent imaging system this is equal to

$$I_i = \left|\mathcal{F}^{-1}\left[circ(NA\cdot k)T\left(k_x-k_0\alpha_i,k_y-k_0\beta_i\right)\right]\right|^2, \tag{2}$$

where the $circ$ function is a circular mask of radius $NA\cdot k_0$ and $T\left(k_x-k_0\alpha_i,k_y-k_0\beta_i\right)$ is the spectrum of the object shifted by the wavevector of the illumination.

FPM is based on recording a series of images captured under different illumination angles (α_i,β_i), chosen such that there is significant overlap between individual image passbands. The information contained within these individual images is combined using iterative phase retrieval[5], in which the real space amplitude of the corresponding region of the estimated object spectrum is replaced by the square root of the captured image. This procedure is carried out for all captured images in the sequence and then repeated for several iterations to recover an estimate of the extended object spectrum. An inverse Fourier transform of the result yields a high-resolution image with a spatial resolution determined by the effective synthetic NA of the FPM system, $NA_{syn} = NA_{obj} + max(\{NA_i\})$, where NA_{obj} is the NA of the objective lens and $max(\{NA_i\})$ is the NA corresponding to the maximum off axis illumination angle.

2.2 FPM system hardware image reconstruction

To capture image data we built an FPM system based on a upright light microscope (Fig. 1(a-b))[6]. This simple microscope comprises a set of low magnification objective lenses mounted on a manually rotatable lens turret, a tube lens (achromatic doublet with a 200 mm focal length) and a large format (15 megapixel) digital camera (IRIS 15, Photometrics). The system has a field of view of 4.8 mm x 2.8 mm with a 4x objective lens (UPLSAPO, Olympus) and 1 mm x 0.6 mm with a 20x objective lens (MPLNFLN, Olympus). Illumination is provided by an array of 22 x 22 individually addressable RGB LEDs (WS2812) mounted below the sample controlled using an ESP32-based microcontroller. The microcontroller stores the illumination sequence and allows flexible display of different patterns. A TTL trigger signal from the camera (high during the global exposure period of the camera's rolling shutter) is used to control display and advance of LED illumination patterns. Image acquisition is ultimately limited by the frame rate of the camera (30 frames per second at full frame), however in practice

we find an exposure time of ~ 100 ms is necessary to ensure a sufficient signal-to-noise ratio for recovery of high-quality images. For an illumination sequence comprising 225 LEDs arranged in a circular pattern centred on the optic axis, this corresponds to a total image acquisition time of ~ 30 seconds per colour channel. Following acquisition, images were reconstructed using a version of the sequential Gauss-Newton phase retrieval algorithm described by Tian et al.[5] to yield an extended estimate of the object spectrum (Fig. 1(c)).

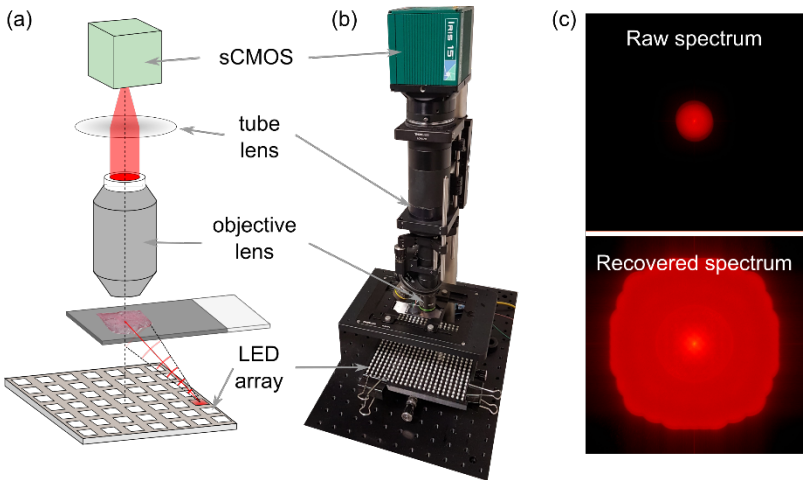

Figure 1 FPM system hardware. (a) Schematic diagram showing the principal hardware components. (b) Photograph of the system. (c) Example spectra (log magnitude) of raw (4x) image (top) and recovered object spectrum (bottom).

3. OPTIMISATION OF IMAGING PERFORMANCE

In order to optimize our system for imaging of clinical samples we carried out a series of simulations using both synthetic and experimentally derived datasets. Effective removal of background signal in the darkfield (DF) images, which typically comprise the majority of an FPM dataset, is particularly important for recovery of high-quality reconstructed images. As described previously uncorrected DF background, arising from stray light and camera dark current, gives rise to a high frequency 'orange peel' artefact which masks the underlying structure of the object. In principle this can be corrected by subtracting a suitable background value from the raw images, however establishing an appropriate value is complicated by the presence of noise. If the subtracted level is too low the orange peel artefact is not fully removed, if it is too high real sample information is removed from the DF images which reduces the spatial resolution and contrast of the reconstructed image. For imaging relatively sparse, well separated objects (such as cells in a thin peripheral blood film) we have found that a non-parametric 'structure dependent amplification' method is effective[7]. In this approach data redundancy in real space is exploited to create maps to retain useful information in DF images whilst suppressing the background. However, in highly unstructured samples such as tissue sections, where object segmentation is challenging, a different approach is required. Figure 2(a) shows how the scaling of the background, measured as the mean pixel value within a manually identified object-free region of interest, affects the accuracy of the reconstructed images using an experimental FPM dataset (H&E-stained 5 μm thick liver tissue section) captured on our system. To quantify the accuracy of the reconstruction we compute the root mean squared error (RMSE) between the raw images and the corresponding low resolution images computed from the recovered complex object using an FPM forward imaging model. Our results suggest that in this case a background scaling factor of 1.4 give optimal results. Based on the distribution of pixel values this corresponds to removal of approximately 92% of all background pixels.

Another important factor in determining both the rate of convergence of the reconstruction algorithm and the quality of the reconstructed images is the overlap between adjacent FPM passbands. This in turn is determined by the size of the objective passband (NA_{obj}/λ) and the difference in illumination angle between adjacent LEDs[8]. A larger overlap fraction (increased data redundancy in Fourier space) can be expected to give better final results. However, to maintain NA_{syn}, and overall spatial

resolution, this comes at the expense of more raw images, and an increase in image acquisition and reconstruction time. In order to explore how passband overlap affects imaging performance we simulated an FPM image series corresponding to our hardware configuration using a synthetic complex test object. A noise free forward imaging model was applied to generate low resolution FPM images corresponding to LED matrix to sample distances from 87 mm to 32.5 mm (overlap of 69% to 23% for the on axis LED and those immediately adjacent) with a fixed illumination sequence. We define with the accuracy of the recovered high-resolution amplitude image as the RMSE compared to the ground truth amplitude. As the LED illumination pattern is fixed then $max(\{NA_i\})$ and NA_{syn} also change with the spacing between LEDs and the sample. This reflects the constraints of a practical FPM system where LEDs are arranged at discrete positions in a rectilinear array and fine tuning of the passband overlap is typically achieved by changing the distance. The results, shown in Fig. 2(b), show a sharp decrease in RMSE as the overlap increases to 40%. This result is similar to the requirement for a 35% minimum passband overlap reported by Dong et al.[9]. As the overlap percentage increases beyond this, the RMSE continues to drop near linearly, however considerably more slowly. It may be expected that the presence of noise in real datasets will even more strongly favour a large passband overlap and for this reason we adopt a large overlap percentage (~70%) for our experimental setup.

Finally, we consider the use of spatial multiplexing to increase image acquisition speed. In conventional FPM each raw image is captured with the sample illuminated by a single LED (generating a single shifted information passband). However, multiplexed strategies in which multiple LEDs are illuminated simultaneously and each image contains information from several non-overlapping passbands have also been proposed[10]. Spatial multiplexing reduces the number of images required to capture the full set of information passbands and increases the irradiance at the sample, reducing the camera exposure time required for a given signal-to-noise ratio. We simulated multiplexed illumination corresponding to two, and four simultaneous LEDs from a conventional (singleplex) experimental FPM dataset of a 5 μm thick H&E stained prostate tissue section. As the LEDs are mutually incoherent each multiplexed image was created by adding together individual images, with non-overlapping passbands from the singleplex dataset. Images were then reconstructed as described by Tian et al.[10], where the estimated real space amplitude is updated for an extended region of the object spectrum (corresponding to the number of passbands) in each cycle of the phase retrieval algorithm. Figure 2(b) shows how the error in the reconstructed amplitude varies with the number of simultaneous LEDs, where (as previously) the RMSE error is computed from the measured low-resolution images and the corresponding images computed from the recovered high-resolution object. Visually we obtain reasonable recovered images in all cases, however the RMSE increases approximately linearly with the number of simultaneously illuminated LEDs. Further, although acquisition time is reduced as fewer raw images are required, we found the total image reconstruction time was comparable for singleplex and multiplex acquisitions.

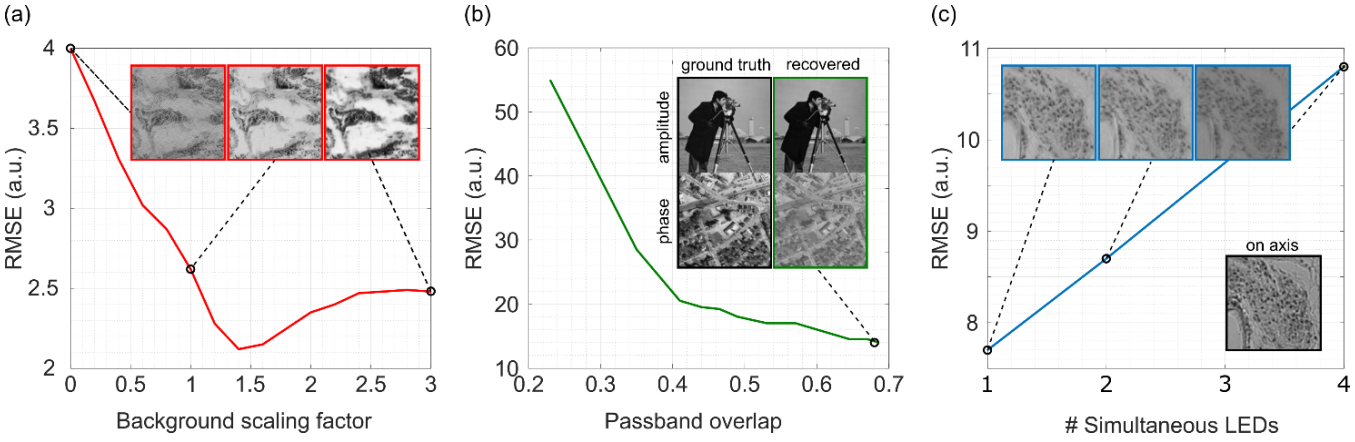

Figure 2. Effect of FPM hardware configuration and reconstruction parameters on accuracy of reconstructed images. (a) Root mean squared error (RMSE) of recovered on axis amplitude image versus level of background subtracted for FPM images of an H&E stained liver tissue section. (b) RMSE of recovered high-resolution amplitude estimate versus percentage overlap between adjacent passbands for our system hardware. (c) RMSE versus number of LEDs which are illuminated in each raw image frame. For (a) and (c) RMSE is calculated from low resolution images computed from the recovered high-resolution object and the corresponding measured images. For (b) the recovered high-resolution amplitude is compared directly against the known amplitude of the synthetic object. Insets show example amplitude images recovered using the parameters indicated by the circles on the plotted curves.

4. IMAGING RESULTS FOR CLINICAL SAMPLES

To test the performance of our FPM system we captured example images of two different classes of clinical samples used for medical diagnosis. For FPM imaging of peripheral blood films we used a 10x/0.3 objective lens, a sample-LED distance of 62 mm (corresponding to a passband overlap of 75% and NA_{syn} of 0.9). DF background signals were corrected using the method described by Claveau et al.[7]. For imaging histological tissue sections we used a 4x/0.16 objective, a sample-LED distance of 87 mm (corresponding to a passband overlap of 69% and NA_{syn} of 0.7). For each DF image the background signal was corrected by subtracting the 1.4 times the mean signal measured in a region of interest free from tissue. In both cases images were captured using sequential (singleplex) illumination of the sample with 225 individual LEDs contained within a circular region of LED matrix centred on the optic axis of the microscope.

Figure 3 shows part of a Giemsa-stained blood film imaged using our setup. Different red blood cell (RBC) morphologies are clearly visible with some cells exhibiting a spiculated shape characteristic of echinocytes and acanthocytes whereas others have a rounded morphology. The zoomed views in the figure insets clearly illustrate that these fine features are not resolved in the corresponding low-resolution amplitude image. For blood films imaged using an air objective lens, individual RBCs present with a dark halo around the edge; in contrast this dark halo is not visible for RBCs imaged using an oil immersion objective due to refractive index matching between the oil and the film[11]. Similarly, we find that white blood cells (WBCs), the internal structure of which is poorly resolved in the low-resolution amplitude image, are imaged effectively using FPM. The nuclear morphology, important for distinguishing between different cell types for a differential WBC count is clearly revealed in the reconstructed amplitude image. The detailed morphology of both RBCs and WBCs is also visible in the inset phase images. Many of the RBCs appear darker in the centre, corresponding to a smaller difference in optical path length due to their biconcave shape. The clear phase difference between RBCs and the background can facilitate intensity-based cell segmentation, however we note that this is reliant on robust 2D phase unwrapping. Phase wrapping artefacts tend to be more prevalent for images captured using an air, rather than oil immersion, objective and both the insets contain phase unwrapping artefacts.

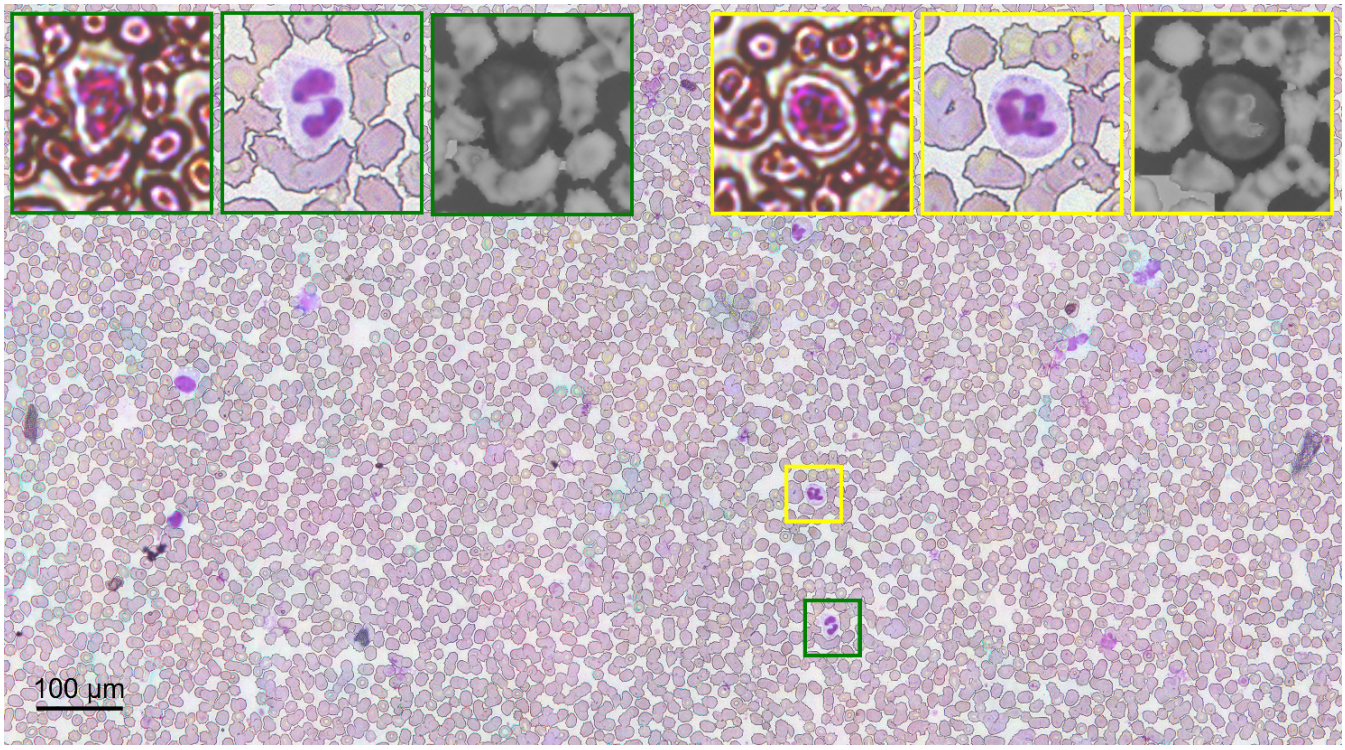

Figure 3. Colour FPM image of a Giemsa-stained blood film captured using 10x/0.3 objective lens. Insets show (from left to right) zoomed views of low resolution on axis amplitude, high-resolution amplitude and high-resolution phase of the boxed regions in the main image.

Figure 4 shows FPM images of 5 µm thick formalin fixed paraffin embedded prostate tissue sections captured using our FPM microscope system (Fig. 1(b)). Figure 4(a) is a raw low-resolution image of an H&E-stained prostate section captured under on axis illumination with a red LED, illustrating the large field of view of the system. The expanded views of the right-hand side of the main panel illustrate how the apparent sizes of individual haematoxylin-stained nuclei are reduced in the recovered high resolution amplitude image due to the increased spatial resolution. The FPM image also allows individual nuclei to be resolved in parts of the tissue where they are densely clustered. We note that although depth of field of the raw image (~8.5 µm) is large enough to contain the entire thickness of the tissue, this is not the case for the reconstructed FPM images where the depth of field is reduced to ~ 1 µm due to the increased effective NA (0.9). As we have shown in previous work[6], the complex object recovered by FPM can be digitally refocused post capture without loss of quality within the depth of field of the objective lens. For visualizing the entire section thickness, a 2D in focus image can be rendered from a computer-generated focal series (z-stack) using an extended depth of field algorithm. Figure 4(b) shows an example high-resolution colour FPM amplitude image of an H&E-stained prostate tissue section where image sequences were captured using sequential illumination with red, green and blue LEDs. To reconstruct colour images we

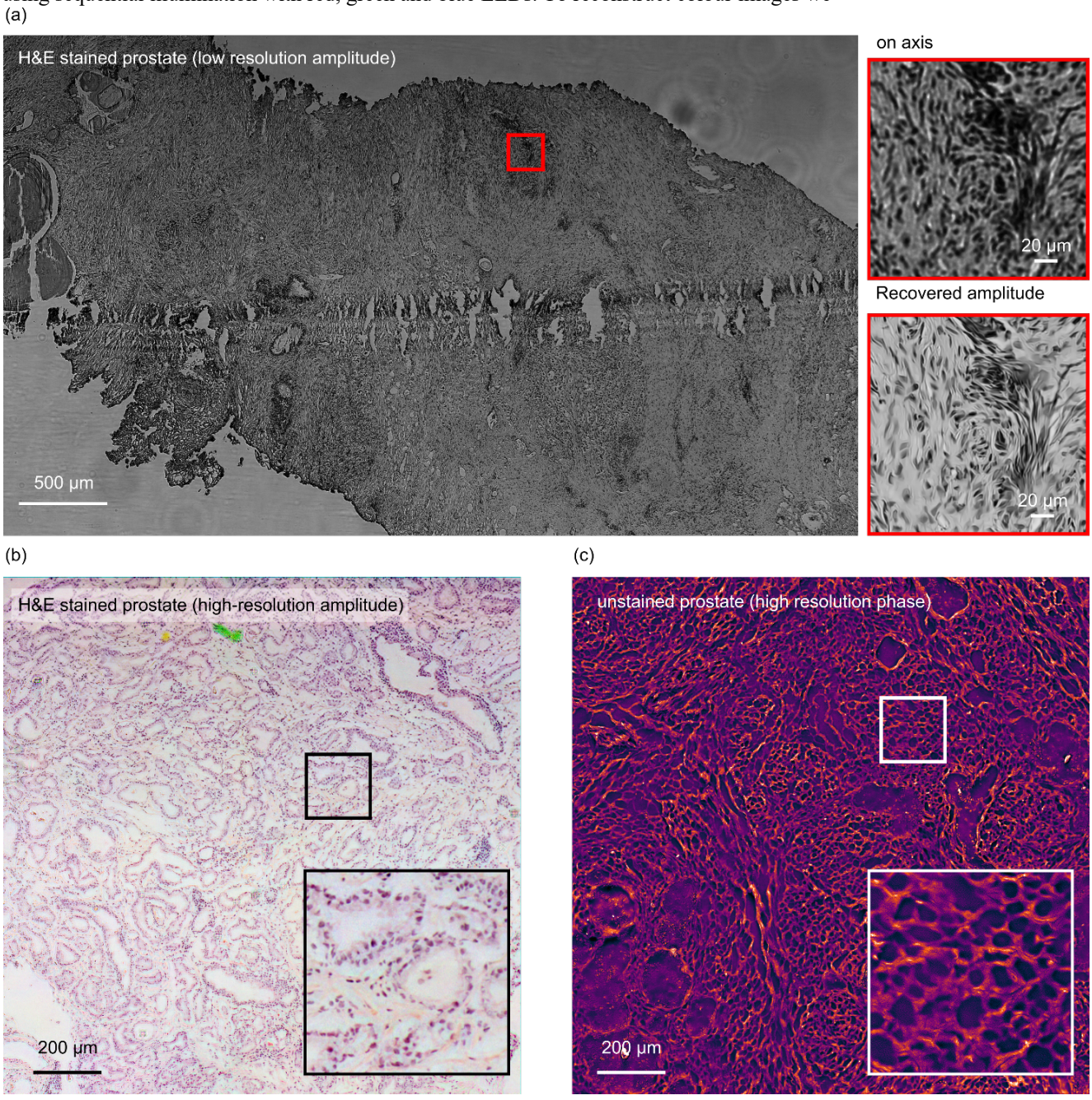

Figure 4. Example FPM images of histological tissue sections. (a) Raw monochrome brightfield image showing full field of view of the FPM system (4.8 mm x 2.8 mm with a 4x objective lens). Insets show zoomed in view of raw (top) and recovered high resolution amplitude (bottom). (b) High-resolution FPM RGB amplitude image of an H&E stained prostate tissue section. (c) False colour high-resolution FPM phase image of a section of unstained prostate tissue.

find it is particularly important to incorporate a defocus term into the pupil function during image reconstruction process[12] to correct for chromatic focus shift between the different colour channels. In addition, after reconstruction individual colour channel images are spatially registered to correct for lateral chromatic offsets before white balancing. Finally, Fig. 4(c) shows a recovered high-resolution phase image of an unstained tissue section. Despite the lack of exogenous staining, differences in the optical path length of the tissue enable clear visualization of the tissue architecture. We also observe that specific features and objects, such as cell nuclei can be identified in FPM phase images.

5. DISCUSSION

By enabling capture of large format, high-resolution images FPM is particularly attractive for histological and cytological imaging. To convert a standard digital brightfield microscope for FPM requires only the addition of a low-cost LED matrix in the illumination pathway and a simple microcontroller to address it and synchronise the LED switching with image acquisition. Wider adoption of FPM is also supported by the existence of several open-source software packages for image reconstruction[13]. At present FPM image reconstruction is relatively computationally intensive and time consuming, with a full FoV reconstruction often taking several hours on a standard laboratory PC. However, improved computing hardware and the adoption of machine learning approaches[14,15] offer the possibility of speeding this up considerably.

In this article we have restricted our analysis to relatively thin clinical samples. Thicker objects, such as thick tissue sections, create challenges for many optical imaging techniques due to increased light absorption and scattering. FPM also further relies on the assumption that inclined illumination simply shifts the captured region of the object spectrum, which is only valid for thin samples. We have found that this assumption is reasonable provided the sample thickness does not significantly exceed the depth of field of the objective lens[6]. Subject to limits on the degree of light scattering, alternative reconstruction methods have successfully been applied for FPM imaging of 3D samples, however at the cost of further increased computational complexity[16,17]. Finally, we note that it's capacity for high-resolution label free imaging is particularly interesting for clinical applications. In both the examples given above the FPM phase images allowed clear visualization of the sample structure (cell morphology and tissue organization). However, phase images typically lack the specificity afforded by exogenous stains and further research is need to explore the wider diagnostic relevance of label-free FPM.

ACKNOWLEDGEMENTS

The authors thank Gbeminiyi Oyinloye and Biobele J. Brown from the College of Medicine of the University of Ibadan, University College Hospital Ibadan, Nigeria for preparing blood film samples and Dr Alex Freeman and Dr Charles Parker for providing histological tissue sections. This work was supported by a proof of concept grant from the Wellcome/EPSRC Centre for Interventional and Surgical Science (203145Z/16/Z) and a grant from the UK's Engineering and Physical Sciences Research Council, Global Challenges Research Fund (EP/P028608/1).

REFERENCES

[1] Park, Y., Depeursinge, C. and Popescu, G., "Quantitative phase imaging in biomedicine," Nature Photon **12**(10), 578–589 (2018).
[2] Antonio, K. A. and Schultz, Z. D., "Advances in Biomedical Raman Microscopy," Anal. Chem. **86**(1), 30–46 (2014).
[3] Zheng, G., Horstmeyer, R. and Yang, C., "Wide-field, high-resolution Fourier ptychographic microscopy," Nature Photon **7**(9), 739–745 (2013).
[4] Fienup, J. R., "Phase retrieval algorithms: a comparison," Appl. Opt., AO **21**(15), 2758–2769 (1982).

[5] Yeh, L.-H., Dong, J., Zhong, J., Tian, L., Chen, M., Tang, G., Soltanolkotabi, M. and Waller, L., "Experimental robustness of Fourier ptychography phase retrieval algorithms," Opt. Express, OE **23**(26), 33214–33240 (2015).
[6] Claveau, R., Manescu, P., Elmi, M., Pawar, V., Shaw, M., Shaw, M., Shaw, M., Fernandez-Reyes, D., Fernandez-Reyes, D. and Fernandez-Reyes, D., "Digital refocusing and extended depth of field reconstruction in Fourier ptychographic microscopy," Biomed. Opt. Express, BOE **11**(1), 215–226 (2020).
[7] Claveau, R., Manescu, P., Fernandez-Reyes, D., Fernandez-Reyes, D., Fernandez-Reyes, D., Shaw, M., Shaw, M. and Shaw, M., "Structure-dependent amplification for denoising and background correction in Fourier ptychographic microscopy," Opt. Express, OE **28**(24), 35438–35453 (2020).
[8] Sun, J., Chen, Q., Zhang, Y. and Zuo, C., "Sampling criteria for Fourier ptychographic microscopy in object space and frequency space," Opt. Express, OE **24**(14), 15765–15781 (2016).
[9] Dong, S., Bian, Z., Shiradkar, R. and Zheng, G., "Sparsely sampled Fourier ptychography," Opt. Express, OE **22**(5), 5455–5464 (2014).
[10] Tian, L., Li, X., Ramchandran, K. and Waller, L., "Multiplexed coded illumination for Fourier Ptychography with an LED array microscope," Biomed. Opt. Express, BOE **5**(7), 2376–2389 (2014).
[11] Shaw, M., Claveau, R., Manescu, P., Elmi, M., Brown, B. J., Scrimgeour, R., Kölln, L. S., McConnell, G. and Fernandez-Reyes, D., "Optical mesoscopy, machine learning, and computational microscopy enable high information content diagnostic imaging of blood films," The Journal of Pathology **255**(1), 62–71 (2021).
[12] Ou, X., Zheng, G. and Yang, C., "Embedded pupil function recovery for Fourier ptychographic microscopy," Opt. Express, OE **22**(5), 4960–4972 (2014).
[13] Rogalski, M., Zdańkowski, P. and Trusiak, M., "FPM app: an open-source MATLAB application for simple and intuitive Fourier ptychographic reconstruction," Bioinformatics(btab237) (2021).
[14] Nguyen, T., Nguyen, T., Xue, Y., Li, Y., Tian, L., Tian, L. and Nehmetallah, G., "Deep learning approach for Fourier ptychography microscopy," Opt. Express, OE **26**(20), 26470–26484 (2018).
[15] Zhang, J., Xu, T., Shen, Z., Qiao, Y. and Zhang, Y., "Fourier ptychographic microscopy reconstruction with multiscale deep residual network," Opt. Express, OE **27**(6), 8612–8625 (2019).
[16] Horstmeyer, R., Chung, J., Ou, X., Zheng, G. and Yang, C., "Diffraction tomography with Fourier ptychography," Optica, OPTICA **3**(8), 827–835 (2016).
[17] Chowdhury, S., Chen, M., Eckert, R., Ren, D., Wu, F., Repina, N. and Waller, L., "High-resolution 3D refractive index microscopy of multiple-scattering samples from intensity images," Optica, OPTICA **6**(9), 1211–1219 (2019).